JOM, Vol. 71, No. 5, 2019
https://doi.org/10.1007/s11837-019-03426-7
© 2019 The Minerals, Metals & Materials Society

TECHNICAL ARTICLE

Effect of Tungsten Doping on the Properties of In_2O_3 Films

R. RESHMI KRISHNAN,[1] V.S. KAVITHA,[1] S.R. CHALANA,[1]
RADHAKRISHNA PRABHU,[2] and V.P. MAHADEVAN PILLAI[1,3]

1.—Department of Optoelectronics, University of Kerala, Thiruvananthapuram, Kerala, India. 2.—School of Engineering, Robert Gordon University, Aberdeen, UK. 3.—e-mail: vpmpillai9@gmail.com

Highly crystalline tungsten oxide (WO_3)-doped indium oxide (In_2O_3) films are synthesized at room temperature by the RF magnetron sputtering technique. The structural and morphological properties of the as-deposited films and the films annealed at a temperature of 300°C are investigated in detail. X-ray diffraction analysis reveals the presence of a cubic bixbyite structure with preferred orientation along the (222) plane for both the as-deposited and annealed films. Moderate WO_3 doping (1 wt.%) enhances the crystallinity of the as-deposited In_2O_3 films, whereas the crystallinity of the films systematically decreases with an increase in WO_3 doping concentration beyond 1 wt.%. Raman spectral analysis discloses the modes of the cubic bixbyite In_2O_3 phase in the films. Atomic force microscopy micrographs show a smooth and dense distribution of smaller grains in the films. X-ray photoelectron spectroscopy reveals the existence of W^{5+} in the doped films. The undoped film is highly oxygen deficient. Variation in the concentration of oxygen vacancy can be associated with the degree of crystallinity of the films.

INTRODUCTION

Metal oxide materials on the nanoscale have emerged as vital components in micro-/nanoscale devices because of their astounding physical and chemical properties, which are dependent on their shape, size/dimensionality, morphology, crystallographic orientation, high transmittance/reflective properties, high conductivity, wide band gap, etc.[1–3]. Among these, indium oxide (In_2O_3) and indium oxide-based thin films have great technological applications owing to their various fascinating aspects including high visible transparency, good electrical conductivity, long-term stability and increased catalytic properties.[4–6] Apart from their widespread applications in electrooptic modulators, low-emissivity windows, solar cells, flat-panel displays, gas sensors, electrochromic mirrors, etc.,[7–9] impurity-added In_2O_3 is found to be suitable for dilute magnetic semiconductors for spintronic applications.[10,11] In_2O_3 can exist in two different crystal structures, namely, a cubic bixbyite structure and rhombohedral structure.[12] In_2O_3 films prepared using different deposition methods may be single crystalline-like or polycrystalline, but they mostly possess the cubic bixbyite structure independent of the substrate used.[13] The cubic bixbyite In_2O_3 structure is thermodynamically stable, while the rhombohedral phase is the metastable phase.[14,15] The formation of rh-In_2O_3 requires high temperature and pressure conditions.[12] Intrinsic defects (oxygen vacancies, interstitials, etc.) in the undoped film can alter its properties. Doping with a suitable dopant material is one of the ways to improve its properties.[16] Tungsten (W) with a lower ionic radius and higher oxidation state compared with an In^{3+} cation can be a good dopant for the In_2O_3 lattice. It is reported that tungsten-doped indium oxide films have high electron mobility, low electrical resistivity and high transparency in the visible and near infrared region.[17–22] Structural properties can affect the quality of thin films thereby modifying their optical, electrical and sensing properties, etc. Thus, these characteristics play a prime role in the technological point of view as these are needed to fabricate films with the desired properties.[23] To the best of our knowledge, there are no reports on the effect of the tungsten oxide (WO_3) doping concentration on the structural properties of RF-sputtered In_2O_3 films prepared at room temperature in argon (Ar) ambience. Yan et al. reported the effect of RF power on tungsten and titanium-doped

In_2O_3 films fabricated using RF magnetron sputtering at room temperature.[24] They also studied the changes in the structural and electrical characteristics of the vacuum post-annealed films. By reactive plasma deposition, Lu et al.[25] synthesized W-doped In_2O_3 films at room temperature for different oxygen/argon (O_2/Ar) ratios. The influence of annealing temperature on the structural, electrical and optical properties was also investigated.[25] Pan et al. reported the role of sputtering power and thickness on the structural, morphological and optoelectrical properties of W-doped In_2O_3 films at room temperature using reactive magnetron sputtering.[20] Samatov et al.[22] investigated the effect of the tungsten doping percentage and fraction of O_2 dilution in the sputtering gas on the optoelectrical and structural properties of RF-sputtered In_2O_3 films. The free electron concentration generated by the dopant tungsten and due to oxygen vacancies was also studied. Amorphous W-doped In_2O_3 films exhibiting smooth surface morphology were reported.

This article reports an in-depth analysis of the role of WO_3 doping on the structural and morphological properties of highly crystalline RF-sputtered In_2O_3 films at room temperature. Also, the effect of annealing at a temperature of 300°C on the properties of In_2O_3 films is investigated. Structural and morphological analyses were performed using techniques such as x-ray diffraction (XRD), micro-Raman spectroscopy, x-ray photoelectron spectroscopy (XPS) and atomic force microscopy (AFM).

EXPERIMENT

WO_3-doped In_2O_3 films were fabricated by the sputtering technique (RF magnetron). In_2O_3 powder (99.99% purity) was mixed with WO_3 powder (99.99% purity in the desired proportions, namely 0 wt.%, 1 wt.%, 2 wt.%, 3 wt.% and 4 wt.%), and the well-ground mixtures were used as sputtering targets. The deposition was carried out in a chamber evacuated to a base pressure of 4×10^{-6} mbar and under an argon pressure of 0.015 mbar for 40 min with an RF power of 120 W (magnetron power supply, Advanced Energy, MDX 500). The films were deposited on quartz substrates kept at a distance of 5 cm from the target. The as-deposited films with WO_3 doping concentrations (viz., 0 wt.%, 1 wt.%, 2 wt.%, 3 wt.% and 4 wt.%) are coded as IW0, IW1, IW2, IW3 and IW4, respectively. The films with different WO_3 doping concentrations are annealed in air at a temperature of 300°C for a duration of 1 h in a controlled programmable furnace with a heating rate of 3 degrees per minute, and the annealed films are coded as IW0(300), IW1(300), IW2(300), IW3(300) and IW4(300), respectively. Both the as-deposited and annealed films are used for characterization.

The structure of the films was studied using an x-ray diffractometer (Bruker AXS D8 Advance) using an x-ray wavelength of 1.5406 Å (Cu Kα1 radiation). The measurements were done in the 2θ range of 20°–70° using Bragg–Brentano geometry at a scan rate of 0.02° per minute. Raman spectra of the film samples were obtained using a Labram HR-800 micro-Raman spectrometer (Horiba Jobin Yvon). An excitation radiation of 514.5 nm from the argon ion laser was employed to record the spectra. A Bruker-Dimension Edge atomic force microscope (Si tip on the nitride lever having a 0.4 N/m force constant) in ScanAsyst mode was used for surface profiling of the films. The oxidation states of the elements are estimated by an XPS spectrometer (Omicron Technology) with a monochromatic AlKα (1486.7 eV) x-ray source. CASA XPS software was used for the XPS data analysis.

RESULTS AND DISCUSSION

Figure 1 shows the XRD patterns of the as-deposited WO_3-doped In_2O_3 thin films with different levels of WO_3 doping. As evidenced by the presence of intense peaks, XRD patterns suggest a polycrystalline nature for all the films. Earlier reports show that In_2O_3 films crystallize only at a temperature of $\sim$ 150°C.[26] The deposition temperature is monitored using a thermo-couple and shows that the temperature in the chamber during deposition was between 40°C and 50°C. It is interesting to note that in the present study, the as-deposited films, though they are deposited on an unheated quartz substrate, possess good crystalline quality. In sputtering systems, the sputtered particles may have a high kinetic energy value ($\sim$ several eV), and this may increase the surface migration of the particles to reach the substrate effectively to produce crystalline films.[27] Park et al.[28] reported that continuous energetic ion bombardment can be the source of crystallization of films on unheated substrates.

The XRD pattern of the IW0 film presents an intense peak at 2θ = 30.66°, a medium intense peak at 51.12° and five weak peaks at 2θ values 21.55°, 41.95°, 45.76°, 59.09° and 60.14°. These peaks belong to the cubic bixbyite structure of In_2O_3 and can be indexed to lattice reflection planes (222), (440), (211), (332), (431), (541) and (622), respectively (JCPDS file no. 71-2195). The presence of the hump-like structure in the 2θ range 20–30° and less intensity of the XRD peaks indicate the less crystalline nature of the undoped film. WO_3 doping in the In_2O_3 lattice seems to have a profound effect on its crystallinity, which is quite evident from the intensity modification in the XRD patterns. The XRD intensity exhibited by the doped films is much higher than that of the undoped film. In all the as-deposited films, the (222) peak shows the highest intensity indicating that <111> is the preferred direction of growth of crystallites in them.

A moderate doping of WO_3 (i.e., 1 wt.%) enhances the crystalline quality of the film drastically as evidenced by the very high intensity in the XRD pattern (Fig. 3a). The intensities of the (222) peak in

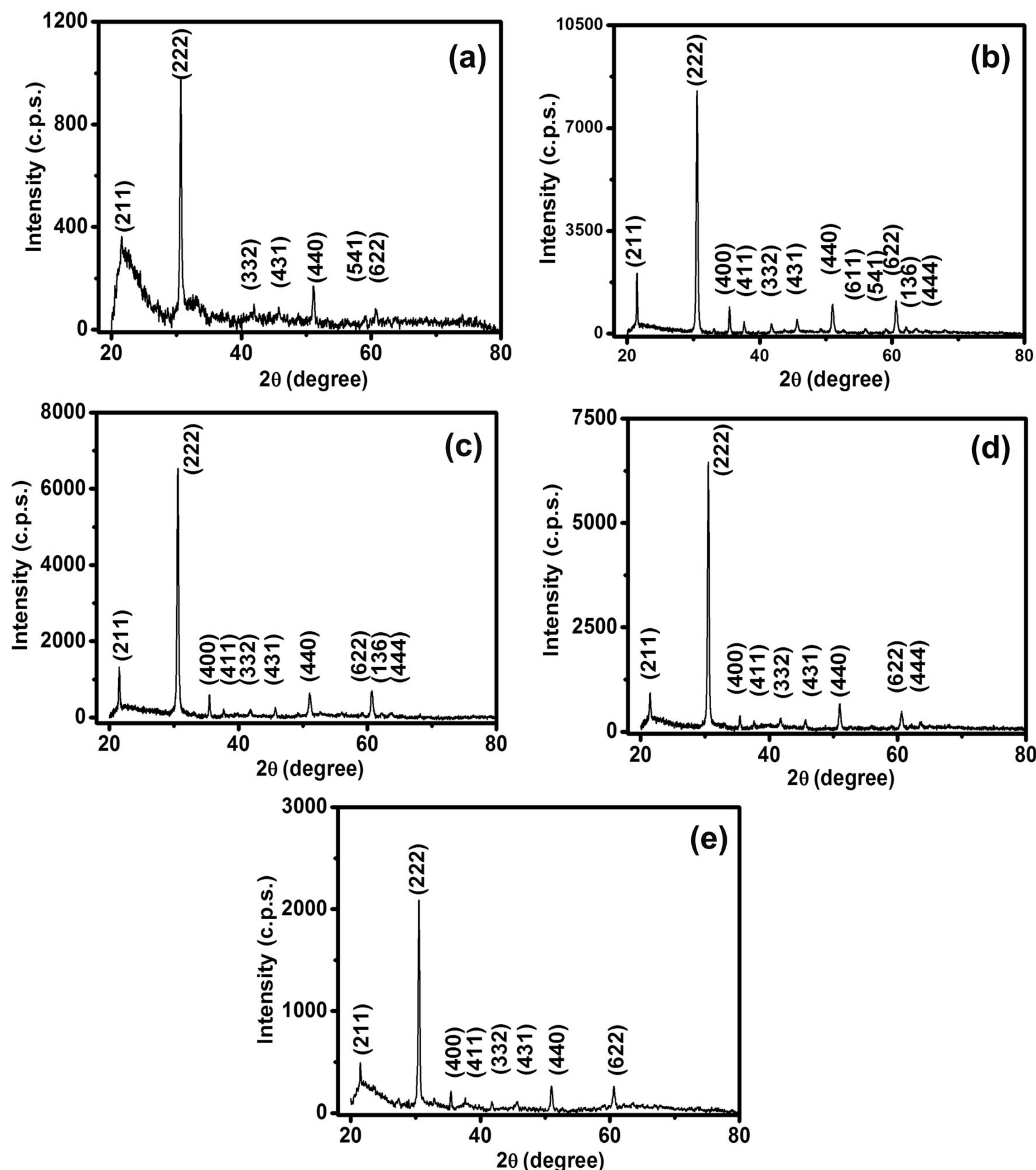

Fig. 1. XRD patterns of as-deposited WO_3-doped In_2O_3 films deposited on the quartz substrate by RF magnetron sputtering technique: (a) IW0, (b) IW1, (c) IW2, (d) IW3 and (e) IW4.

IW1, IW2, IW3 and IW4 are respectively 8.70, 6.86, 6.69 and 2.13 times that of IW0 film. This indicates that WO_3 doping in the In_2O_3 lattice improves its crystallinity even under the as-deposited condition, and the crystallinity of the IW1 film is superior compared with other films.

Figure 2 represents the XRD patterns of WO_3-doped films annealed at a temperature of 300°C. All the peaks in the XRD patterns of the annealed films can be indexed to the cubic bixbyite phase of In_2O_3. Also, in the annealed films <111> is the preferred direction of crystalline growth. Annealing of the films in air for 1 h at 300°C enhances the intensity of the most intense peak (222) compared with that in the as-deposited counterparts (Fig. 3a). Some additional peaks are also observed in the XRD patterns of all the annealed films. The enhancement in the XRD peak intensities as well as the appearance of additional peaks in the annealed films indicates an improvement in the crystallinity compared with the as-deposited films.

Among the as-deposited films, the IW0 film shows the least value of the XRD peak intensity. On annealing, the intensity of the (222) peak (IW0 film) is enhanced by 6.25 times compared with that of the as-deposited film. In the as-deposited film, there

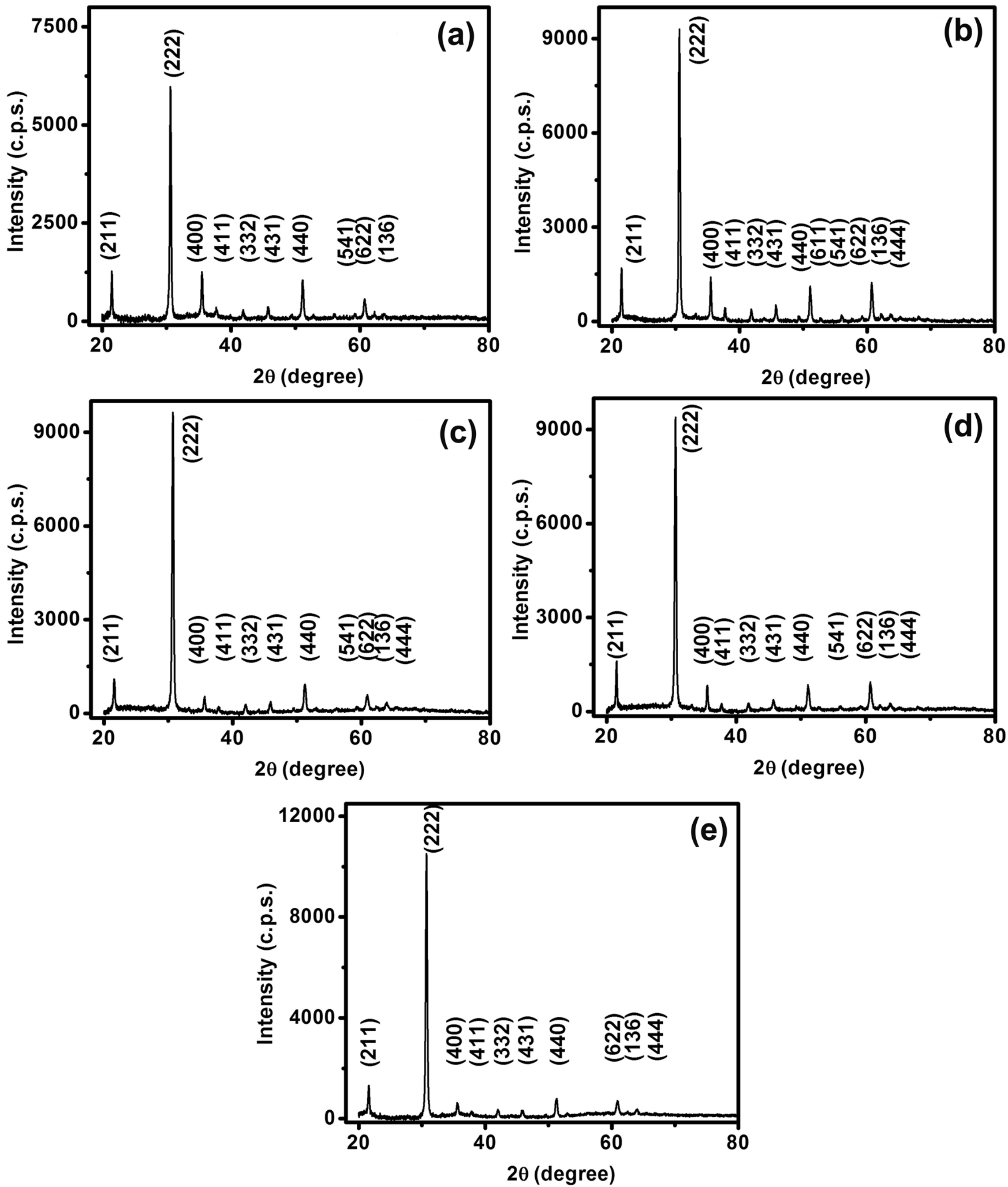

Fig. 2. XRD patterns of WO_3-doped In_2O_3 films annealed at a temperature of 300°C: (a) IW0(300), (b) IW1(300), (c) IW2(300), (d) IW3(300) and IW4(300).

may be defects due to oxygen vacancy and other lattice disorders. On thermal annealing, oxygen vacancies get filled, lattice disorders decrease, stoichiometry improves and hence crystallinity increases. Compared with In_2O_3, WO_3 is an oxygen-rich entity. Doping of In_2O_3 with WO_3 can provide more oxygen to the lattice, and oxygen vacancies get filled, and the film becomes more stoichiometric. This can be the reason for the improvement in crystallinity of the WO_3-doped In_2O_3 films in the as-deposited conditions. On thermal annealing, the stress gets released and defects may get reduced. Among the annealed films, IW4(300) film shows the highest intensity. The intensity of the (222) peak in IW4(300) film is about 5.09 times that of the IW4 film. Among all the films, IW4(300) film shows superior crystalline quality.

In the IW0 film, the (222) peak is observed at a 2θ value 30.66°. In the doped as-deposited films, this peak shifts to lower 2θ values (Fig. 3b). In the IW0(300) film, the (222) peak is observed at a 2θ value of 30.623°. In the IW0(300) film, this peak

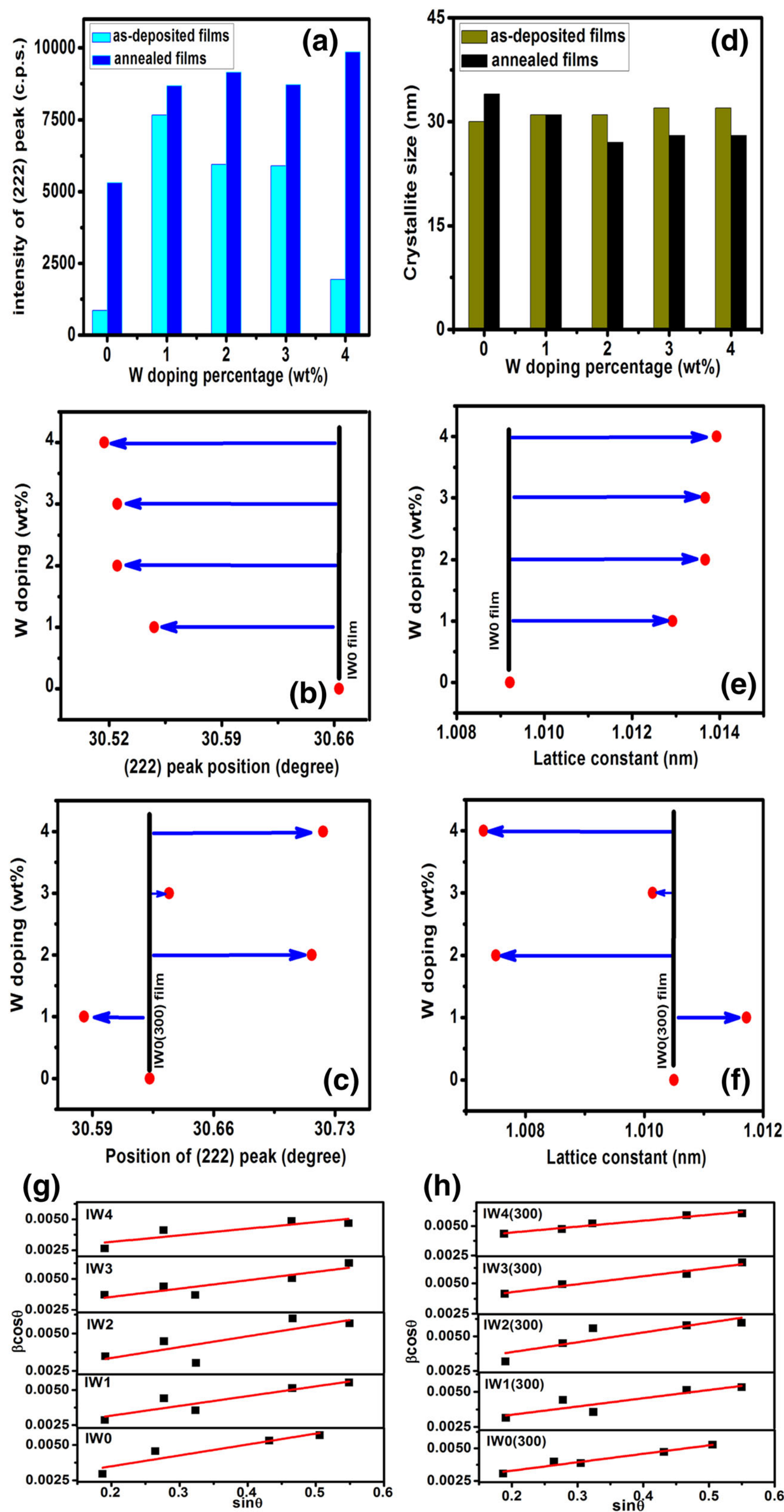

Fig. 3. (a) Variation of intensity of (222) peak in the as-deposited and annealed films with WO_3 doping concentration, variation of position of (222) peak with WO_3 doping concentration for: (b) as-deposited films and (c) annealed films, (d) variation of crystallite size in the as-deposited and annealed films with WO_3 doping concentration, variation of lattice constant with WO_3 doping concentration in: (e) as-deposited films and (f) annealed films. Williamson-Hall (W-H) plot of WO_3 doped In_2O_3 films: (g) as-deposited films and (h) films annealed at a temperature of 300°C.

shifts to lower 2θ values, while in other doped annealed films, this peak shifts to higher 2θ values (Fig. 3c).

The lattice constant 'a' for a cubic system is calculated from the interplanar spacing d of the intense (222) peak by the following relation:[29]

$$\frac{1}{d^2} = \frac{h^2 + k^2 + l^2}{a^2} \quad (1)$$

where h, k and l are the Miller indices. The calculated values of the lattice constant for the as-deposited and annealed films are shown in Fig. 3e and f, respectively, and Table I. In the as-deposited films, the value of the lattice constant increases because of WO_3 doping compared with undoped IW0 film. However, in the annealed doped films, the value of the lattice constant decreases except for the IW1(300) film compared with the IW0 film. In the IW1(300) film, the lattice constant shows a slight increase compared with the IW0 film. The ionic radii of the different tungsten ions are: W^{4+}– 0.066 nm,[25] W^{5+}– 0.062[30] and W^{6+}– 0.060 nm.[25] For all these tungsten ions, the ionic radii are less than those of indium (In) ions (In^{3+}– 0.081 nm).[31] The crystal lattice contracts and lattice constant decreases when dopant ions of smaller radii are substituted for host ions of larger radii.[32] However, in the as-deposited films, the observed values of lattice constant are not in line with this argument. The enhancement of the lattice constant suggests an expansion of the lattice. Meng et al.[33] observed higher values of the lattice constant for molybdenum (Mo)-doped In_2O_3 films although the ionic radius of Mo^{6+} (0.062 nm) is smaller than that of In^{3+} ions (0.081 nm).[33] Shukla et al.[34] also observed an expansion of the lattice when zinc oxide (ZnO) is doped with Al^{3+} ions of lower ionic radii (0.53 Å) compared with that of Zn^{2+} ions (0.72 Å) for higher doping levels. They attributed this to the possibility of having Al^{3+} ions in the interstitial position. The lattice mismatch, strain effects and mismatch among the ions, impurities and defects can also lead to expansion of the lattice.[35–37] Since the films are as-deposited, the dopant ions may not have sufficient energy to diffuse into the appropriate In^{3+}sites. However, in the annealed films except for the IW1(300) film, the lattice constant shows lower values suggesting a contraction of the lattice and substitution of In^{3+} sites by tungsten ions. On annealing, tungsten ions may get sufficient energy to diffuse into the appropriate In^{3+} sites and get substituted. Also, thermal annealing reduces the defects and strain effects in the film. The value of the lattice constant observed for IW1(300) film is 1.0117 nm, almost identical to the bulk In_2O_3 [1.0118 nm, JCPDS file no. 71-2195]. All the doped films annealed at 300°C show a lower lattice constant value compared with their as-deposited analogs.

Table I. Structural parameters of as-deposited and annealed WO_3-doped In_2O_3 films on a quartz substrate by RF magnetron sputtering

WO_3 doping level (wt.%)	Lattice constant (nm)		Crystallite size (nm)				Lattice strain from W-H plot	
			As-deposited films		Annealed films			
	As-deposited films	Annealed films	From Scherrer formula	From W–H plot	From Scherrer formula	From W–H plot	As-deposited films	Annealed films
0	1.0092 ± 0.0255	1.0105 ± 0.0241	30 ± 1.15	71 ± 27	34 ± 1.44	70 ± 13	0.0037 ± 0.0010	0.0032 ± 0.0377
1	1.0129 ± 0.0219	1.0117 ± 0.0229	31 ± 1.49	85 ± 30	31 ± 1.49	67 ± 25	0.0039 ± 0.0010	0.0033 ± 0.0009
2	1.0137 ± 0.0212	1.0075 ± 0.0276	31 ± 1.56	77 ± 40	27 ± 0.93	61 ± 28	0.0041 ± 0.0017	0.0040 ± 0.0012
3	1.0137 ± 0.0212	1.0101 ± 0.0245	32 ± 1.61	67 ± 17	28 ± 1.13	49 ± 06	0.0038 ± 0.0010	0.0037 ± 0.0452
4	1.0139 ± 0.0210	1.0073 ± 0.0279	32 ± 1.63	70 ± 22	28 ± 0.95	42 ± 02	0.0030 ± 0.0012	0.0028 ± 0.0294

The mean value of the size of the crystallites D_{hkl} can be calculated by employing the following Scherrer equation using the peak position ($2\theta_{hkl}$) and the full width at half maximum in radians (β_{hkl}):[38]

$$D_{hkl} = \frac{0.9\lambda}{\beta_{hkl}\cos\theta_{hkl}} \quad (2)$$

Here λ is the x-ray wavelength. The calculated values of crystallite size in the as-deposited and annealed films are listed in Table I, and the observed size suggests the nanostructured nature of the films. The effect of WO_3 doping and thermal annealing on the mean size of the crystallites is illustrated in Fig. 3d.

The reduction in the size of the crystallites and strain in the films can broaden the XRD peaks. The strain free crystallite size (D'_{hkl}) can be determined by using the Williamson–Hall (W–H) plot analysis by the following relation:[39]

$$\beta_{hkl}\cos\theta_{hkl} = \frac{k\lambda}{D'_{hkl}} + 2\eta\sin\theta_{hkl} \quad (3)$$

where θ_{hkl} is half of the diffraction angle, k is the correction shape factor, which can be taken as 0.9 for spherical grains, and η is the residual strain. W–H plots for the as-deposited and annealed WO_3-doped In_2O_3 films are shown in Fig. 3g and h. The crystallite size and strain in the films are estimated from the linear fit of $\beta\cos\theta$ versus $\sin\theta$. The size of the crystallites and strain can be evaluated from the y-intercept and slope, respectively. The dissimilarity in the crystallite size estimated using the Scherrer formula and W–H plot (Table I) manifests the presence of strain-induced peak broadening in the films.

Crystalline oxide thin films have wide applications in flat-panel displays, light-emitting diodes, solar cells, etc.[40] Our study found that the annealed films have better crystalline quality than the as-deposited films. Therefore, the annealed WO_3-doped films can be suitable for the afore-mentioned applications. Although amorphous oxide films are reported to have high transparency to visible light, good uniformity and low process temperature, they suffer instability issues due to stress and environmental conditions, such as light, humidity, temperature, etc., during device operation.[41] Increasing the crystallinity, the device stability can be improved considerably.[41] The occurrence of stress/strain in coatings and thin films is a major concern in many technological applications as excessive stress/strain values can affect the reliability and performance of components/devices.[42] Large levels of stress/strain may lead to film cracking or affect the adhesion of the films to the substrate, affecting the performance of components in aerospace and optoelectronic devices.[42] Also, stress/strain in nanostructures and thin films can have a useful impact on their physical properties such as conductivity, dielectric permittivity, enhancement in carrier mobility in Si-based semiconductor technology, etc.[42] Among the deposited films, IW4(300) film has good crystalline quality and a low strain value. Hence, this film with good structural properties is a possible candidate for optoelectronic device applications.

The thickness of the as-deposited and annealed films is estimated from the cross-sectional field emission scanning electron microscopy (FESEM) images. For the as-deposited films, the thickness is in the range 270–371 nm, whereas for the annealed films, it is in the range 243–297 nm.

The vibrational analyses of the as-deposited and annealed WO_3-doped In_2O_3 films are done using micro-Raman spectroscopy. The micro-Raman spectra of WO_3-doped In_2O_3 films without annealing are shown in Fig. 4a. Two very-low-frequency sets at 103 cm^{-1} and 130 cm^{-1}, two low-frequency sets at 302 cm^{-1} and 366 cm^{-1} and two high frequency sets at 494 cm^{-1} and 629 cm^{-1} are reported as the vibrational modes for cubic bixbyite In_2O_3 phase by Gan et al.[43] The presence of these modes in the Raman spectra of all the films supports the formation of the cubic bixbyite In_2O_3 crystalline phase.[44] The band $\sim$ 132 cm^{-1} in the undoped and doped films can be assigned to the vibration of the In-O bond emerging from the InO_6 structural unit.[43] This mode shows the highest intensity in the IW1 film. The medium intense $\sim$ 307 cm^{-1} band can be related to the $\delta(InO_6)$ bending vibration of InO_6 octahedra.[45] The weak band at 368 cm^{-1} can be assigned to the stretching vibrations of In-O-In, which manifest the presence of oxygen vacancies in the structure.[46] The stretching vibrations $\nu(InO_6)$ of the InO_6 octahedron result in the occurrence of $\sim$ 495 cm^{-1} and 628 cm^{-1} bands.[45,46] The $\sim$ 604 cm^{-1} and 830 cm^{-1} bands may have emerged from the quartz substrate.[47,48] All the expected vibrational modes of the cubic bixbyite In_2O_3 structure are observed with moderate intensity in the Raman spectrum of the IW1 film. Also, the vibrational modes obtained for the IW1 film are narrower compared with other WO_3-doped films. This shows the better crystalline quality of the IW1 film compared with others.

The micro-Raman spectra of WO_3-doped In_2O_3 films annealed at a temperature of 300°C are shown in Fig. 4b. The spectra of all the films show sharper and more intense bands compared with those of the as-deposited films. This supports the improved crystalline nature of the annealed films.

Figure 5 depicts the typical 2D AFM micrographs of as-deposited and annealed WO_3-doped In_2O_3 films. The AFM images of all the films reveal a smooth, dense distribution of smaller grains. The IW1 film presents slightly bigger grains compared with others. The AFM image of the IW4 film shows the distribution of grains of two different sizes due to a tendency of agglomeration of crystallites in some regions of the film. In the IW4(300) film, the grains are of almost same size. The root mean

square (rms) surface roughness values calculated using WSxM 5.0 develop 6.4 software[49] are found to be in the range 1.25–2.98 nm for the as-deposited films and in the range 1.63–2.27 nm for the annealed films. AFM analysis reveals a smooth surface morphology for all the films, which is beneficial for optoelectronic applications.

The chemical states of the elements in as-deposited WO_3-doped In_2O_3 films are studied by XPS analysis. The acquired binding energies are calibrated using the C 1*s* peak (284.8 eV).[50] In 3*d* core-level spectra of IW0, IW1 and IW4 films (Fig. 6a, b and c, respectively) exhibit the spin orbital splitting resulting in In $3d_{5/2}$ and In $3d_{3/2}$ peaks.[51] CASA XPS software is used to fit the peaks in the core level spectra. In $3d_{5/2}$ and In $3d_{3/2}$ peaks are observed at 444.38 eV and 451.97 eV, respectively, in the XPS spectrum of IW0 film. These peaks are observed at 444.51 eV and 452.08 eV, respectively, for the IW1 film and at 444.38 eV and 451.95 eV, respectively, for the IW4 film. The difference in binding energy of In $3d_{5/2}$ and In $3d_{3/2}$ in these films is found to be 7.57 eV, which is in agreement with reported values.[52,53] A slight shift in In $3d_{5/2}$ and In $3d_{3/2}$ peaks to higher binding energy positions is observed for the IW1 film.

The O 1*s* core level spectra of IW0, IW1 and IW4 films are shown in Fig. 6d, e and f, respectively. For the films, deconvolution of the peak in the O 1*s* region yields two components—a low binding energy component O(I) and high binding energy component O(II). Beena et al. obtained two components in the O 1*s* spectra ~ 529.49 eV and 531.05 eV for In_2O_3 films prepared at a substrate temperature of 300 K.[54] For undoped film, O(I) can be related to oxygen in the In_2O_3 lattice,[55] and for WO_3 doped films, O(I) can be related to oxygen in the In_2O_3 or WO_3 lattice.[56,57] O(II) can be correlated with oxygen in oxygen-deficient regions.[54,58] For the undoped film IW0, the components are centered at 529.49 eV (O(I)) and 531.38 eV (O(II)). O(I) and O(II) peak positions of the IW1 film are at 530.02 eV and 531.68 eV, respectively, and for the film IW4, these peaks are at 529.73 eV and 531.51 eV, respectively. The O 1*s* peaks in the WO_3-doped films are observed at relatively higher binding energy positions compared with those in IW0 film. The intensity of O(I) and O(II) peaks and the area ratio (O_{II}/O_I) for the films IW0, IW1 and IW4 are given in Table II.

The values of intensities of O(I) and O(II) peaks show considerable variation with the WO_3 doping concentration. The value of the intensity of the O(I) peak is highest for the IW1 film and lowest for the IW0 film. The intensity of the O(II) peak is lowest for the IW1 film and highest for the IW0 film. The intensity variation of the O(II) peak can be an indication of the variation of the concentration of oxygen vacancies in the films. For the films IW0, IW1 and IW4, the area ratio $\left[{}^{O(II)}/_{O(I)}\right]$ is found to

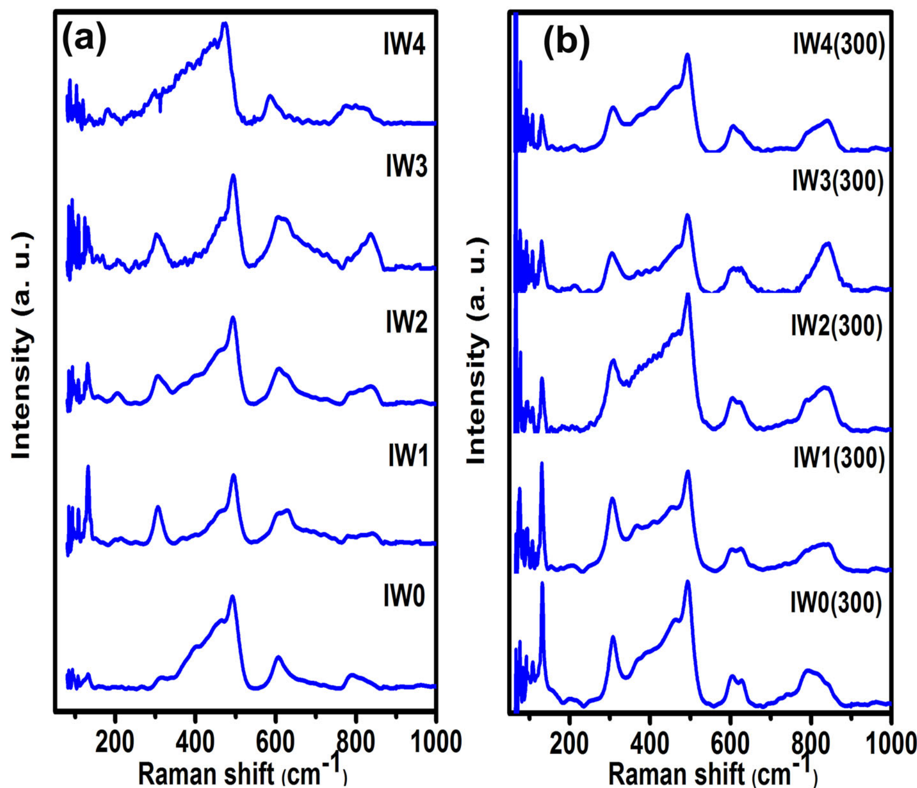

Fig. 4. Micro-Raman spectra of WO_3-doped In_2O_3 films on the quartz substrate by RF magnetron sputtering technique: (a) as-deposited and (b) annealed at 300°C.

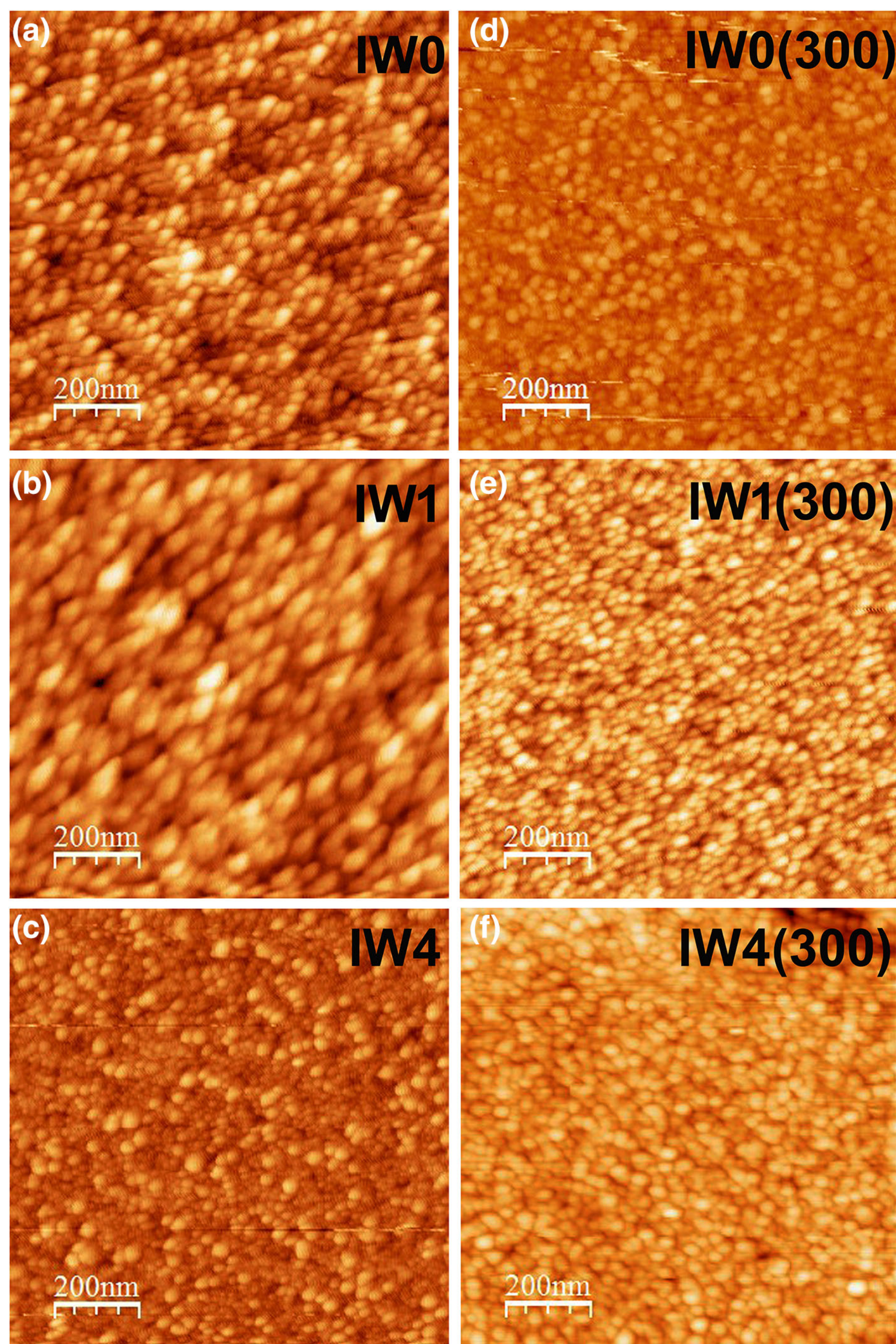

Fig. 5. Two-dimensional AFM images of typical WO_3-doped In_2O_3 films: as-deposited films (a) IW0, (b) IW1 and (c) IW4 and annealed films (d) IW0(300), (e) IW1(300) and (f) IW4(300).

be 3.43, 1.11 and 2.03, respectively. The high value of the area ratio manifests the presence of many oxygen vacancies.[59,60] In the present case, this ratio is higher for the undoped film compared with the doped films IW1 and IW4. This implies that the undoped film is highly oxygen deficient. Among the doped films, $\left[{}^{O(II)}/_{O(I)}\right]$ is the lowest for the IW1 film, and this indicates a reduction in the concentration of oxygen vacancies in this film. In indium zinc oxide films, Kumar et al.[61] reported a decrease in the area ratio $\left[{}^{O(II)}/_{O(I)}\right]$ with an increase in the atomic ratio [Zn/(Zn + In)]. They attributed this decrease to the enhancement in film crystallinity with an increase in the atomic ratio. For zinc (Zn)-doped In_2O_3 nanopyramids, Bartolome et al. observed an increase in the lower binding energy component of oxygen (O(I)) in the regions with a high Zn concentration and attributed this to the

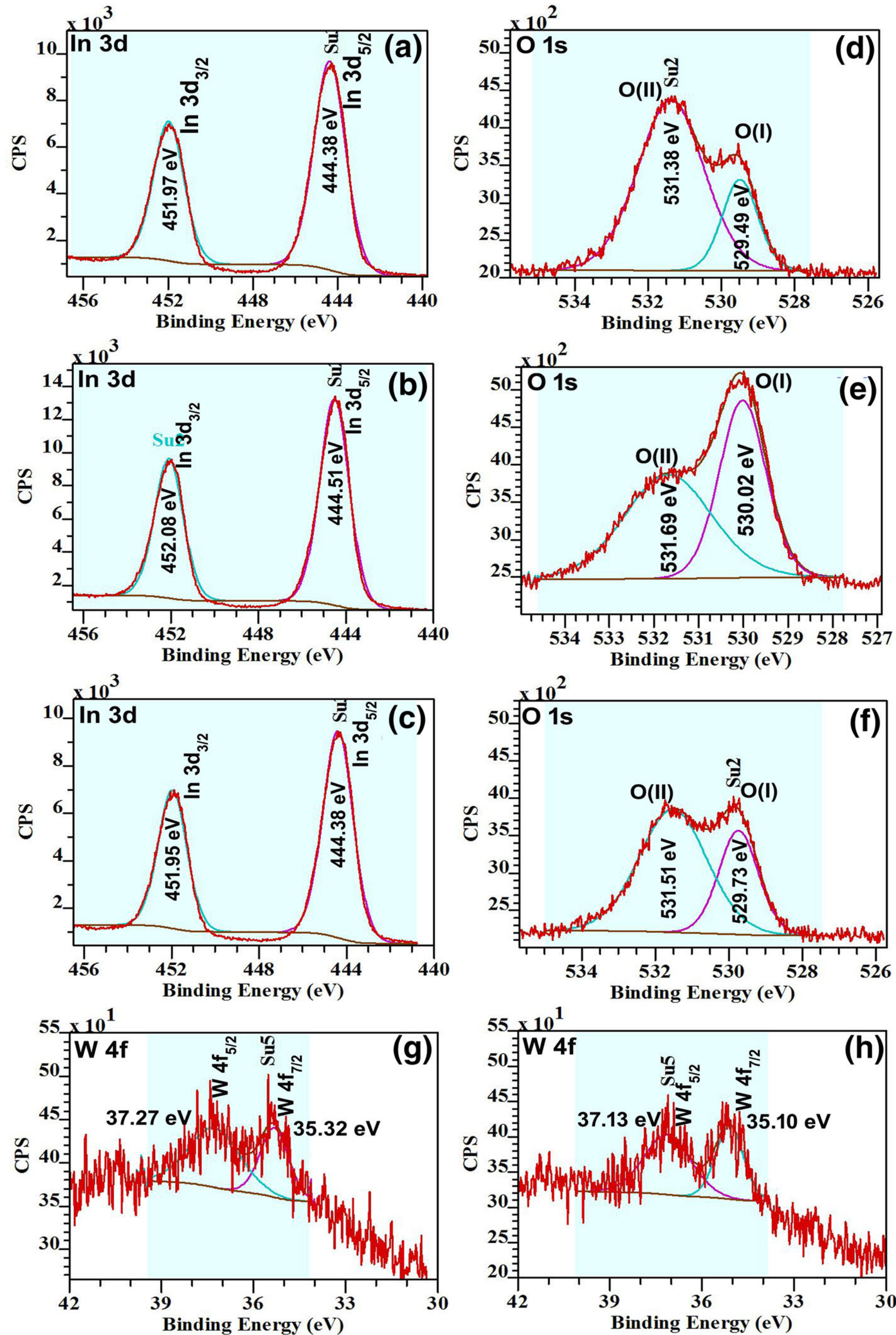

Fig. 6. In the 3d core level spectra of typical as-deposited WO_3-doped In_2O_3 films deposited by the RF magnetron sputtering technique: (a) IW0, (b) IW1 and (c) IW4. O 1*s* core level spectra of typical as-deposited WO_3-doped In_2O_3 films: (d) IW0, (e) IW1 and (f) IW4. W 4f XPS spectra of typical as-deposited WO_3-doped In_2O_3 films: (g) IW1 and (h) IW4.

crystallinity improvement with increasing Zn concentration.[62] The increase in the concentration of the O(I) component and the low value of the area ratio observed for the IW1 film imply an improvement in crystallinity of this film, which is in accordance with the XRD analysis. An enhancement in the intensity of In 3*d* peaks is also observed for the IW1 film compared with other doped films. The reduction in the O(I) component and the increase in the area ratio for the IW4 film support the declination in crystallinity at higher doping concentration.

Figure 6g and h shows the W 4*f* core level spectra of the typical WO_3-doped In_2O_3 films, IW1 and IW4, respectively. By the deconvolution of the W 4*f* peak, a doublet is obtained with binding energies of 35.32 eV and 37.27 eV for the IW1 film and 35.10 eV and 37.13 eV for the IW4 film,

Table II. Binding energy positions of In, O and W components, intensities of oxygen components and area ratio of high energy peak (O_{II}) to a low energy peak (O_I) of O 1*s* from XPS data for typical as-deposited WO_3-doped In_2O_3 films: IW0, IW1 and IW4

	Binding energy positions (eV)								
Sample code	In $3d_{5/2}$	In $3d_{3/2}$	O(I)	O(II)	W $4f_{7/2}$	W $4f_{5/2}$	O(I) (%)	O(II) (%)	Area ratio O(II)/O(I)
IW0	444.38	451.97	529.49	531.38	–	–	22.57	77.43	3.43
IW1	444.51	452.08	530.02	531.68	35.32	37.27	47.46	52.54	1.11
IW4	444.38	451.95	529.73	531.51	35.10	37.13	32.90	67.10	2.03

respectively. The higher binding energy component at 37.27 eV observed for the IW1 film and that at 37.13 eV for the IW4 film (Fig. 6g and h) can be ascribed to the W $4f_{5/2}$ level. The lower binding energy component at 35.32 eV for the film IW1 and that at 35.10 eV (Fig. 6g and h) for the IW4 film can be attributed to the W $4f_{7/2}$ level. These peaks indicate the presence of tungsten in the +5 oxidation state.[63] For the IW4 film, a slight shift in the positions of the W $4f_{5/2}$ and W $4f_{7/2}$ peaks toward lower binding energy is observed compared with that of the IW1 film.

CONCLUSION

The present study focuses on the effect of WO_3 doping and annealing at a 300°C on the structural and morphological properties of In_2O_3 films synthesized at room temperature. XRD and Raman analysis reveals that both the as-deposited films and annealed films possess a cubic bixbyite structure and exhibit a strong preferred orientation along the (222) plane. WO_3 doping and post-annealing of the films have a profound effect on the crystallinity of the In_2O_3 films. The deposition of films with smooth morphology is illustrated by AFM images. Incorporation of tungsten in the In_2O_3 lattice is supported by XPS analysis. XPS analysis reveals the presence of the W^{5+} state in the WO_3-doped films.

REFERENCES

1. W. Ahmed, *Nanomaterials and Nanotechnology* (Manchester: One Central Press (OCP) Ltd, 2016).
2. V. Patil, S. Pawar, M. Chougule, P. Godse, R. Sakhare, S. Sen, and P. Joshi, *J. Surf. Eng. Mater. Adv. Technol.* 1, 35 (2011).
3. S.S. Batros and G.S. Karam, *Int. J. Comput. Eng. Res. (IJCER)* 4, 15 (2014).
4. S. Hashmi, *Comprehensive Materials Processing* (USA: Elsevier Inc., 2014), p. 77.
5. O. Kamoun, A. Boukhachem, C. Mrabet, A. Yumak, P. Petkova, K. Boubaker, and M. Amlouk, *Bull. Mater. Sci.* 39, 777 (2016).
6. G. Korotcenkov, V. Brinzari, and B.K. Cho, *Int. J. Electr. Comput. Eng.* 10, 884 (2016).
7. A. Murali, A. Barve, V.J. Leppert, and S.H. Risbud, *Nano Lett.* 1, 287 (2001).
8. K. Sreenivas, T.S. Rao, A. Mansingh, and S. Chandra, *J. Appl. Phys.* 57, 384 (1985).
9. Z. Fang, H. Assaaoudi, R.I.L. Guthrie, J.A. Kozinski, and I.S. Butler, *J. Am. Ceram. Soc.* 90, 2367 (2007).
10. A. Tiwari, V.M. Bhosle, S. Ramachandran, N. Sudhakar, J. Narayan, S. Budak, and A. Gupta, *Appl. Phys. Lett.* 88, 142511 (2006).
11. Y.A.E. Aoud, M.C. Hickey, A.G. Kussow, and A. Akyurtlu, *Phys. Status Solidi A* 210, 2644 (2013).
12. ChY Wang, Y. Dai, J. Pezoldt, B. Lu, Th Kups, V. Cimalla, and O. Ambacher, *Cryst. Growth Des.* 8, 1257 (2008).
13. S. Richter and A. Schwedt, *EMC 2008: Materials Science* (Berlin: Springer Science & Business Media, 2008).
14. A. Walsh and C.R.A. Catlow, *J. Mater. Chem.* 20, 10438 (2010).
15. I. Hotovy, T. Kups, J. Hotovy, J. Liday, D. Buc, M. Caplovicova, V. Rehacek, H. Sitter, C. Simbrunner, A. Bonnani, and L. Spiess, *J. Electr. Eng.* 61, 382 (2010).
16. A.E. Fakir, M. Sekkati, G. Schmerber, A. Belayachi, Z. Edfouf, M. Regragui, F.C. El Moursli, Z. Sekkat, A. Dinia, A. Slaoui, and M. Abd-Lefdil, *Phys. Status Solidi C* 14, 1700169 (2017).
17. X. Li, Q. Zhang, W. Miao, L. Huang, and Z. Zhang, *Thin Solid Films* 515, 2471 (2006).
18. Y. Abe and N. Ishiyama, *Mater. Lett.* 61, 566 (2007).
19. D.R. Acosta and A.I. Martínez, *Thin Solid Films* 515, 8432 (2007).
20. J. Pan, W. Wang, D. Wu, Q. Fu, and D. Ma, *J. Mater. Sci. Technol.* 30, 644 (2014).
21. P.F. Newhouse, C.-H. Park, D.A. Keszler, J. Tate, and P.S. Nyholm, *Appl. Phys. Lett.* 87, 112108 (2005).
22. I.G. Samatov, B.R. Jeppesen, A.N. Larsen, and S.K. Ram, *Appl. Phys. A* 122, 458 (2016).
23. E. Parsianpour, D. Raoufi, M. Roostaei, B. Sohrabi, and F. Samavat, *Adv. Mater. Phys. Chem.* 7, 42 (2017).
24. L.T. Yan and R.E.I. Schropp, *Thin Solid Films* 520, 2096 (2012).
25. Z. Lu, F. Meng, Y. Cui, J. Shi, Z. Feng, and Z. Liu, *J. Phys. D Appl. Phys.* 46, 75103 (2013).
26. S. Muranaka, Y. Bando, and T. Takada, *Thin Solid Films* 151, 355 (1987).
27. P.K. Song, Y. Shigesato, M. Kamei, and I. Yasui, *Jpn. J. Appl. Phys.* 38, 2921 (1999).
28. J.-O. Park, J.-H. Lee, J.-J. Kim, S.-H. Cho, and Y.K. Cho, *Thin Solid Films* 474, 127 (2005).
29. B.D. Cullity, *Elements of X-Ray Diffraction* (Boston: Addison-Wesley Publishing Company Inc, 1956).
30. A. Kafizas and I.P. Parkin, *J. Am. Chem. Soc.* 133, 20458 (2011).
31. M.R. Pai, J. Majeed, A.M. Banerjee, A. Arya, S. Bhattacharya, R. Rao, and S.R. Bharadwaj, *J. Phys. Chem. C* 116, 1458 (2012).
32. V. Sharma, A. McDannald, M. Staruch, R. Ramprasad, and M. Jain, *Appl. Phys. Lett.* 107, 012901 (2015).
33. Y. Meng, X. Yang, H. Chen, J. Shen, Y. Jiang, Z. Zhang, and Z. Hua, *Thin Solid Films* 394, 219 (2001).
34. R.K. Shukla, A. Srivastava, A. Srivastava, and K.C. Dubey, *J. Cryst. Growth* 294, 427 (2006).
35. H. Kim, J.S. Horwitz, S.B. Qadri, and D.B. Chrisey, *Thin Solid Films* 420–421, 107 (2002).
36. H. Kim, A. Piqué, J.S. Horwitz, H. Murata, Z.H. Kafafi, C.M. Gilmore, and D.B. Chrisey, *Thin Solid Films* 377–378, 798 (2000).

37. R. Eason, *Pulsed Laser Deposition of Thin Films* (New Jersey: Wiley, 2007), p. 682.
38. A.L. Patterson, *Phys. Rev.* 56, 978 (1939).
39. G.K. Williamson and W.H. Hall, *Acta Metall.* 1, 22 (1953).
40. H. Kozuka, M. Takahashi, K. Niinuma, and H. Uchiyama, *J. Asian Ceram. Soc.* 4, 329 (2016).
41. K. Park, H.-W. Park, H.S. Shin, J. Bae, K.-S. Park, I. Kang, K.-B. Chung, and J.-Y. Kwon, *I.E.E.E. Trans. Electron Dev.* 62, 290 (2015).
42. G. Abadias, E. Chason, J. Keckes, M. Sebastiani, G.B. Thompson, E. Barthel, G.L. Doll, C.E. Murray, C.H. Stoessel, and L. Martinu, *J. Vac. Sci. Technol., A* 36, 020801 (2018).
43. J. Gan, X. Lu, J. Wu, S. Xie, T. Zhai, M. Yu, Z. Zhang, Y. Mao, S.C.I. Wang, Y. Shen, and Y. Tong, *Sci. Rep.* 3, 1021 (2013).
44. L. Guo, X. Shen, G. Zhu, and K. Chen, *Sens. Actuators B. Chem.* 155, 752 (2011).
45. S. Elouali, L.G. Bloor, R. Binions, I.P. Parkin, C.J. Carmalt, and J.A. Darr, *Langmuir* 28, 1879 (2012).
46. G.M. Kumar, A.M. Kumar, P. Ilanchezhiyan, and T.W. Kang, *Nanoscale* 6, 11226 (2014).
47. J.W. Chan, T. Huser, S. Risbud, and D.M. Krol, *Opt. Lett.* 26, 1726 (2001).
48. R.S. Krishnan, *Nature* 155, 452 (1945).
49. I. Horcas, R. Fernández, J.M.G. Rodríguez, J. Colchero, J.G. Herrero, and A.M. Baro, *Rev. Sci. Instrum.* 78, 013705 (2007).
50. P. Babelon, A.S. Dequiedt, H. Mostefa-Sba, S. Bourgeois, P. Sibillot, and M. Sacilotti, *Thin Solid Films* 322, 63 (1998).
51. S. Hu, B. Chi, J. Pu, and L. Jian, *J. Mater. Chem. A.* 2, 19260 (2014).
52. B. Ballarin, M.C. Cassani, C. Maccato, and A. Gasparotto, *Nanotechnology* 22, 275711 (2011).
53. W.J. Kim, D. Pradhan, and Y. Sohn, *J. Mater. Chem. A.* 1, 10193 (2013).
54. D. Beena, K.J. Lethy, R. Vinodkumar, V.P.M. Pillai, V. Ganesan, D.M. Phase, and S.K. Sudheer, *Appl. Surf. Sci.* 255, 8334 (2009).
55. Y. An, S. Wang, L. Duan, J. Liu, and Z. Wu, *Appl. Phys. Lett.* 102, 212411 (2013).
56. X.G. Wang, Y.S. Jang, N.H. Yang, L. Yuan, and S.J. Pang, *Surf. Coatings Technol.* 99, 82 (1998).
57. P. Chatchai, Y. Murakami, S. Kishioka, A.Y. Nosaka, and Y. Nosaka, *Acta* 54, 1147 (2009).
58. J.C.C. Fan and J.B. Goodenough, *J. Appl. Phys.* 48, 3524 (1977).
59. S.-H. Kim, H.-S. Choi, and K.-D. Jung, *Cryst. Growth Des.* 16, 1387 (2016).
60. D.V. Shinde, D.Y. Ahn, V.V. Jadhav, D.Y. Lee, N.K. Shrestha, J.K. Lee, H.Y. Lee, R.S. Mane, and S.-H. Han, *J. Mater. Chem. A.* 2, 5490 (2014).
61. B. Kumar, H. Gong, and R. Akkipeddi, *J. Appl. Phys.* 97, 063706 (2005).
62. J. Bartolomé, D. Maestre, M. Amati, A. Cremades, and J. Piqueras, *J. Phys. Chem. C* 115, 8354 (2011).
63. Z. Si, D. Weng, X. Wu, Y. Jiang, and B. Wang, *Catal. Sci. Technol.* 1, 453 (2011).

Publisher's Note Springer Nature remains neutral with regard to jurisdictional claims in published maps and institutional affiliations.